

Fan Flow Deflection for Supersonic Turbofan Engines

Dimitri Papamoschou* and Preben E. Nielsen†

University of California, Irvine, CA, 92697-3975

We present an initial parametric investigation of fan flow deflectors for suppressing noise from supersonic turbofan engines. Realistic exhaust geometry and flow conditions for bypass ratio 2.7 were simulated in a subscale experiment. The study encompassed acoustic measurement and mean velocity surveys. The deflectors comprised internal vanes with both symmetric and cambered airfoil sections and deployable external flaps. Superior acoustic results were achieved using a combination of cambered vanes and perforated flaps, yielding cumulative (downward plus sideline) EPNL and OASPL reductions of 7.7 dB and 9.2 dB respectively. A fair correlation is established between the suppression of peak OASPL and the reduction of the radial velocity gradient on the underside of the jet.

Nomenclature

A	Nozzle exit area
a	Two-dimensional airfoil lift curve slope
C_L	Lift coefficient
c	Vane chord length
D_f	Fan nozzle diameter
f	Frequency
G	Radial velocity gradient
J	Thrust
L	Vane lift
M	Mach number
p	Pressure
r	Radial direction
S	Wedge wetted area
U	Nozzle exit velocity
u	Mean axial velocity in jet plume
w	Average vane span
x	Axial direction
y	Vertical direction
z	Horizontal transverse direction
α	Angle of attack, wedge half angle
γ	Specific heat ratio
ϵ	Turning effort
η	Efficiency
θ	Polar angle
ϕ	Azimuth angle

*Professor, Department of Mechanical and Aerospace Engineering, 4200 Engineering Gateway, Irvine, CA 92697-3975, AIAA Associate Fellow.

†Graduate Researcher, Department of Mechanical and Aerospace Engineering, 4200 Engineering Gateway, Irvine, CA 92697-3975, AIAA Student Member.

Subscripts

<i>LE</i>	Leading edge
<i>p</i>	Primary (core) exhaust
<i>s</i>	Secondary (fan) exhaust
<i>v</i>	Vane
<i>w</i>	Wedge

I. Introduction

THIS research builds upon the previous work performed at U.C. Irvine’s Jet Aeroacoustics Facility into the use of fan flow deflector technology for supersonic jet noise reduction.¹ The earlier studies used simple nozzles and rather crude, external airfoil-type deflectors that are known to induce significant losses. The current study uses realistic nozzle shapes and leverages the advent of new types of deflectors, namely internal vanes and external wedges, developed in subsonic jet noise reduction efforts.^{2,3} Noise reduction is achieved in a coaxial separate-flow turbofan engine by tilting the bypass (secondary) plume downward by a small amount relative to the core (primary) plume. The misalignment of the plumes creates a thick, low-speed region on the underside of the jet which leads to a decrease in the convective Mach number of turbulent eddies in the jet shear layer. This principle, shown in Figure 1, leads to a reduction in the intense noise that propagates to the downward and sideline acoustic far-field.

Supersonic transportation is becoming increasingly viable both technologically and economically. However, a major obstacle continues to be the problem of jet noise and the regulations governing the amount of noise that can be produced near airports. This research aims to develop innovative jet noise reduction techniques for application on future civilian and military supersonic aircraft to facilitate environmental noise compliance. The primary focus of the investigation is on the design, characterization and optimization of methods to reduce overall jet noise radiation towards airport communities. This is achieved through investigation of the interconnected elements of engine cycle, aerodynamic performance and noise reduction through the use of passive-control methods to asymmetrically reshape the exhaust plume. In this investigation fan flow deflectors are used to achieve mean flow distortion of the supersonic jet plume. The aircraft envisioned has a cruise Mach number of 1.6 and weighs in the neighborhood of 9,000 kg. An engine cycle analysis for the determination of optimal noise reduction is summarized and the results of acoustic experiments in conjunction with mean flow analysis of the jet plumes are presented to gain insight into an optimal fan flow deflection configuration.

II. Engine Cycle Analysis

In this section we present a brief overview of the thermodynamic cycle analysis that leads to the determination of the exhaust conditions of the turbofan engine that are simulated in the experiment. The basic turbofan configuration shown in Figure 2 was analysed using a “conventional” gas turbine cycle with provisions for turbine cooling and the ability to compare mixed-flow and unmixed-flow cycles. Table 1 summarizes the component efficiencies and specific heat ratios assumed. Figure 2 shows some of the principal variables involved in the cycle analysis. The purpose of the analysis is to establish reasonable ranges for the bypass ratio (BPR) and fan pressure ratio (FPR) of a state-of-the-art engine that would give acceptable cruise performance while ensuring compliance with takeoff noise regulations.

Figure 3 shows the results of such an exercise. It plots contour maps of thrust specific fuel consumption (TSFC) versus BPR and FPR at cruise (Mach 1.6) conditions for an unmixed-cycle engine with overall pressure ratio $OPR = 15$, rotor inlet temperature $RIT = 1800$ K, and turbine cooling mass flow ratio $R_{cool} = 0.2$. The minimum TSFC occurs at $BPR = 2.2$ and $FPR = 2.7$. Such large FPR would require a two-stage fan. Also, the BPR may be too small for noise compliance. Selecting the point $BPR = 2.7$, $FPR = 2.2$, shown by the red mark on Figure 3, mitigates these concerns without significant increase in TSFC. Of course, the BPR cannot become too large without excessive drag penalties. Therefore, this research focuses on BPR between 2 and 3, and this specific report on $BPR = 2.7$.

Once the engine cycle parameters for cruise are chosen, they are then used to establish the takeoff exit conditions. The “Acoustic Tests” column of Table 2 lists these conditions for $BPR = 2.7$, $FPR = 2.2$, and $RIT = 1800$ K. The conditions are then reproduced in the subscale experiments.

III. Nozzle and Fan Flow Deflectors

The nozzle design in this report is based on the NASA GRC 3BB separate-flow nozzle, nominally for bypass ratio $BPR = 5$. The fan duct was reduced in diameter to produce $BPR = 2.7$ at the conditions of the acoustics tests (Table 2), and the entire nozzle was scaled down by factor of eight to fit within the flow rate capability of the UCI facility. The nozzle design and exit coordinates of the nozzle are shown in Figures 4 and 5. The baseline nozzles were fabricated using a rapid prototyping epoxy method. The fan exit diameter was $D_f=28.1$ mm, and the fan exit height was 1.8 mm. The small fan exit height necessitated the fabrication of vanes of very small dimensions, of the same order as the fan exit height.

Fan flow deflection is achieved through the use of both internal airfoil-shaped vanes and external wedges/flaps as shown in Figure 6. The vanes were micro-machined from high-strength polycarbonate material using CAD/CAM facilities at U.C. Irvine (Roland MDX-40 Subtractive Rapid Prototyping Milling machine). The vane cross sections encompassed symmetric and asymmetric airfoils. The symmetric vanes have a NACA 0012 airfoil cross section while the cambered vanes have a NACA 4412 cross section. The base and tip of each vane are shaped to conform to the geometry of the fan and core ducts at the exact location where the vane is attached. The vane chord length was 3 mm and the vane trailing edge was situated 2 mm upstream of the nozzle exit. Using one-dimensional theory it is estimated that the Mach numbers at the leading and trailing edges of the vane were 0.4 and 0.8, respectively. The external flaps had a length of 10 mm and half angle of 20 deg. They were positioned 5 mm downstream of the fan nozzle exit. The flaps were constructed from a fine metal mesh with a solidity of 50%. Parallel research efforts in high-bypass nozzles have shown that perforated flaps (versus solid flaps or solid wedges) reduce velocity gradients in the vicinity of the deflector, thus reduce the potential of excessive noise created by the deflector itself.⁴

Nozzles were tested with both single-pair and two-pair vane configurations, with and without wedge-type flaps at various azimuthal angles and angles of attack. The particular configurations presented in this discussion are displayed in Table 3. A four-vane configuration with vanes at azimuthal angles of 110 deg and 165 deg and both with an angle of attack of 10 deg is shown in Figure 7.

A number of correlations can be made by investigating the total turning effort of the fan flow deflectors and the effect on the jet noise produced. The turning effort is the total force of the fan flow deflectors normalized by the thrust of the bypass stream and can be viewed as a total deflection angle of the bypass stream from all of the deflectors. The turning effort is thus given by

$$\epsilon = \frac{1}{J_s} \sum_{i=1}^N L_i \quad (1)$$

as a normalised sum of all of the individual vane and wedge lift forces. A computational study by Murayama et al.⁵ for internal vane fan flow deflectors determined that the lift for the internal vane airfoil was the same as an airfoil in external flow when the reference flow conditions were taken at the internal vane leading edge. The lift coefficient for the internal vane is then given by

$$C_L = a\alpha_v \quad (2)$$

where a is the 2-dimensional lift curve slope for the airfoil section used. Taking the flow conditions at the vane leading edge gives the total lift force

$$L_v = a\alpha_v q_{LE} c w \quad (3)$$

as a function of vane angle of attack, dynamic pressure at the vane leading edge q_{LE} , vane chord length c and average vane span w . The aerodynamics of a wedge shaped fan flow deflector were investigated by Papanoschou et al.⁶ which determined the lift force of the wedge given by

$$L_w = C_L(\alpha_w) q_s S \quad (4)$$

where the lift coefficient is dependent on the wedge half angle, the dynamic pressure is taken at the bypass nozzle exit and the wetted area S is determined by the wedge geometry and the material solidity.⁴

The individual lifts of each deflector can be applied in Equation 1 to give the total turning effort ϵ for each fan flow deflector configuration.

IV. Aeroacoustic Testing

Aeroacoustic tests were conducted in U.C. Irvine’s Jet Aeroacoustics Facility, depicted in Figure 8. This is a subscale facility (approximately $1/40^{\text{th}}$ of full scale for the tests in question) that uses helium-air mixtures for simulating the exhaust velocity and density of hot jets.⁷ The exit flow conditions matched the conditions listed in the “Acoustic Tests column of Table 2.

Jet noise was recorded by a microphone array consisting of eight 3.2 mm condenser microphones (Bruel & Kjaer, Model 4138) arranged on a circular arc centered at the vicinity of the nozzle exit. The polar aperture of the array is 30 deg and the array radius is 1 m. The angular spacing of the microphones is logarithmic. The entire array structure was rotated around its center to place the array at the desired polar angle. Positioning of the array is done remotely using a stepper motor. An electronic inclinometer displayed the position of first microphone. Variations of the azimuth angle are possible by rotating the nozzle. This study encompassed the azimuth angles of 0 deg (downward) and 60 deg (sideline).

The arrangement of the microphones inside the anechoic chamber, and the principal electronic components, are shown in Figure 8. The microphones were connected, in groups of four, to two amplifier/signal conditioners (Bruel & Kjaer, Model 4138) with low-pass filter set at 300 Hz and high-pass filter set at 100 kHz. The four-channel output of each amplifier was sampled at 250 kHz per channel by a multi-function data acquisition board (National Instruments PCI-6070E). Two such boards, one for each amplifier, were installed in a Pentium 4 personal computer. National Instruments LabView software was used to acquire the signals.

The sound pressure level spectrum was corrected for actuator response, free-field correction, and atmospheric absorption. The overall sound pressure level (OASPL) was obtained by integrating the corrected spectrum. The sound spectra are corrected for the frequency response of the microphone and for atmospheric absorption. Through an elaborate procedure, the sound measurements are converted into effective perceived noise level (EPNL) measured by ground observation points. A full discussion of the noise calculation process is presented by Papamoschou.² The EPNL is evaluated for a constant-altitude flyover (1500-ft altitude) in the downward ($\phi = 0$ deg) and sideline ($\phi = 60$ deg) directions. In this report the PNL and EPNL are based on an engine thrust of 120.1 kN and an engine angle of attack of 10 deg. SPL spectra at full-scale size are presented by dividing the laboratory frequencies by the scale factor of 44 and are referenced to a distance of $r/D_f=1.25$ from the jet nozzle exit.

V. Mean Velocity Surveys

Each acoustic test was followed by a mean velocity survey in a duplicate dual-stream apparatus. Instead of helium-air mixtures, pure air was used in both primary and secondary streams. Therefore, the flow velocities were lower than those in the acoustic tests. However, the velocity ratio $U_s/U_p = 0.67$, and primary Mach number $M_p = 1.03$, were held the same as in the acoustic tests. The Reynolds number of the jet, based on fan diameter, was 0.92×10^6 in the acoustic tests and 0.47×10^6 in the mean velocity surveys.

The mean axial velocity in the jet plume was surveyed using a Pitot rake system, shown in Figure 9. The rake consists of five 1-mm internal diameter Pitot probes attached to a three dimensional traverse system. The 70 mm long probes are spaced vertically 10 mm apart using a streamlined mounting plate. Each Pitot probe is connected individually to a Setra Model 207 pressure transducer. The pressure was sampled at a rate of 1000 Hz by an analog to digital data acquisition board (National Instruments PCI-MIO-16E). Mach number and velocity were calculated from the Pitot pressure assuming constant pressure (equal to ambient value) and constant total temperature (equal to room temperature).

The three dimensional traverse system consists of three IMS MDrive 23 motor drivers connected individually to THK LM Guide Actuators. The traverse system is run remotely using National Instruments LabView over a pre-specified traverse array. The traverse array typically consisted of 28 axial planes spanning 14 inches, each axial plane comprising 17 horizontal passes of length 101.6 mm spaced 2.5 mm vertically apart. The horizontal passes were made at a speed of 10.16 mm/s.

The data on each y-z plane are interpolated on a fixed grid. The Pitot pressure is converted to velocity under the assumption of constant static pressure (equal to the ambient value) and constant total temperature (equal to room temperature). Smoothing of the velocity profiles, and computation of the velocity gradients, is performed using a Savitzky-Golay filter.

For each axial station, the radial derivatives were calculated on the radial-azimuthal ($r - \phi$) coordinate

system. The origin of the $(r - \phi)$ system is defined as the centroid of the region where the Pitot pressure exceeds 95% of its maximum value. The first and second derivatives were calculated along radial lines from $\phi=0$ to 354 deg in increments of 4 deg. The resulting radial velocity gradient is normalized in the form

$$G(x, r, \phi) = \frac{D_f}{U_p} \frac{\partial u(x, r, \phi)}{\partial r}$$

Of particular interest is the maximum value of the magnitude of the gradient for given x and ϕ ,

$$G_{max}(x, \phi) = \frac{D_f}{U_p} \left| \frac{\partial u(x, r, \phi)}{\partial r} \right|_{max}$$

VI. Aeroacoustic Results

Aeroacoustic results are presented with respect to the baseline nozzle results. Each figure shows narrow-band lossless spectra at various polar angles θ (measured from the jet axis), overall sound pressure (OASPL) versus θ , perceived noise level (PNL) versus time, and PNL versus polar angle. The reductions in EPNL and peak value of OASPL are also shown. These aeroacoustic attributes facilitate a determination of the merit of the various fan flow deflector configurations. As stated previously, 2-, 4- and 6-vane and wedge combination configurations were investigated with both symmetric and cambered vanes and mesh wedges. A number of various configurations are now presented to illuminate the process of the fan flow deflector optimization.

The aeroacoustic results for a configuration consisting of a single pair of symmetric NACA 0012 airfoil vanes at an azimuth angle $\phi = 150^\circ$ and an angle of attack $\alpha = 7.5^\circ$ are shown in Figure 10 and 11 for microphone angles 0 deg and 60 deg respectively as measured from the vertical downward direction. This configuration results in very small downward EPNL and peak-OASPL reductions of 0.4 dB and 0.7 dB respectively and marginally better sideline EPNL and peak-OASPL reductions of 1.2 dB and 1.7 dB respectively. These tests configuration indicate that a small pair of vanes, of the small size used here (approximately 2×3 mm) may not be sufficient to provide significant acoustic reductions.

When an additional pair of symmetric vanes is added a number of changes in the jet noise are realized. Figures 12 and 13 show the aeroacoustic results for a 4-vane configuration with a pair of symmetric NACA 0012 vanes at $\phi = 150^\circ$ and $\alpha = 7.5^\circ$ as before with another pair of symmetric vanes placed at an azimuth angle $\phi = 90^\circ$ with an angle of attack also set at $\alpha = 7.5^\circ$. The downward EPNL and peak-OASPL reductions are improved to 3.4 dB and 3.5 dB respectively. The sideline EPNL and peak-OASPL reductions are improved to 3.1 dB and 3.2 dB, respectively. One deficiency of this configuration is the higher OASPL levels seen at larger polar angles.

Further improvements are seen when cambered vanes are used, which are able to give superior lift-to-drag ratios over the symmetric vanes. Figure 14 and 15 show the aeroacoustic results for a promising 4-vane configuration for microphone angles of 0 deg and 60 deg respectively. This configuration consists of 2 pairs of micromachined vanes with a NACA 4412 cambered airfoil cross section. The top pair of vanes was set at an azimuth angle $\phi = 150$ deg with an angle of attack $\alpha = 4$ deg. The bottom pair were set at $\phi = 90$ deg and $\alpha = 7.5$ deg. This configuration results in good downward EPNL and peak-OASPL reductions of 3 dB and 3.3 dB respectively and very good sideline EPNL and peak-OASPL reductions of 4.1 dB and 3.6 dB respectively. This particular configuration has encouraging attributes as it gives significant spectral reductions at lower polar angles resulting in significant OASPL reductions together with negligible spectral increases at higher polar angles.

A configuration consisting of a single external mesh wedge as shown in Figure 16 gives the acoustic results in Figure 17 and 18 for the downward and sideline microphone angles respectively. Very good downward EPNL and OASPL reductions of 3.9 dB and 4.1 dB respectively are realized whilst giving moderate 2.5 dB and 2.3 dB reductions in the sideline EPNL and OASPL respectively.

A configuration combining two pairs of cambered vanes and a mesh wedge results in further reductions in EPNL and OASPL at both downward and sideline microphone angles. The assembled mesh wedge and micromachined vane configuration is shown in Figure 19. The corresponding acoustic results for the downward and sideline microphone angles are shown in Figure 20 and 21. This configuration results in downward EPNL and peak-OASPL reductions of 4.4 dB and 5.2 dB respectively and sideline EPNL and peak-OASPL reductions of 3.3 dB and 4.0 dB respectively. While there is a minor decrease in the sideline EPNL reduction from the 4-vane configuration due to a slight increase in the spectral levels at higher polar

angles, this is offset by further sideline OASPL reductions. The downward reductions in EPNL and OASPL are very promising and with refinements it is hoped to produce EPNL and OASPL reductions of over 5 dB for both downward and sideline measurements.

In addition to conducting spectral analyses, it is important to also examine statistics in the time domain. The skewness of the fluctuating pressure signal can be utilized to further analyze the reductions evident in all fan flow deflection acoustic measurements. The skewness is defined as

$$\text{Skewness} = \frac{\overline{p'^3}}{\overline{p'}^{\frac{3}{2}}} \quad (5)$$

and has been shown by Ffowcs-Williams et al.⁸ to have direct correlations to the emission of Mach waves and accompanying “crackle” noise. A decrease in the skewness of the pressure signal indicates a relative suppression of Mach wave radiation and hence decreased levels of noise radiated to the far field. Timetraces of the pressure signal for the baseline and 4V+W case are shown in Figure 22 for the polar angle $\theta = 45$ deg. The resulting skewness of the timetraces are calculated according to Equation 5 and are shown in Figure 23. The large reductions in the peak level of skewness of case 4V+W, almost 50% below the baseline, indicates a significant reduction in the emission of Mach waves.

Results from all the acoustic experiments have been analysed to determine the underlying trends in order to find the best configuration. The turning effort of each configuration was determined according to Murayama et al.⁵ and compared to the cumulative maximum EPNL and OASPL reductions from both downward and sideline microphone positions measured in the aeroacoustics facility. The results are presented in Figure 24. A general trend is evident that suggests a positive correlation between turning effort and EPNL and OASPL reduction. It was observed however that placing both the symmetric and cambered micromachined vanes at angles of attack larger than $\alpha = 7.5$ deg resulting in increased noise levels in the broadside direction.

While a general trend of better sound reduction with increased turning effort is present a compromise must be reached due to possible increases in drag especially when the wedge is implemented. It is envisaged that the wedge will be deployable and only used during takeoff when jet noise reduction is required.

VII. Mean Velocity Results

The results for the mean flow of the jets are presented as a composite of the velocity contour for the vertical longitudinal (symmetry) plane, a number of transverse velocity contour plots at various distances downstream and several velocity line plots on the symmetry plane. Figure 25 and 26 display the mean velocity results and the maximum-gradient $G_{max}(x, \phi)$ contours for the baseline nozzle. The velocity isocontours in the two planes presented are fairly axisymmetric and the maximum gradient contours are relatively constant indicating that the nozzle components (fan, core and plug) are in good alignment. The line plots also confirm this symmetry in the vertical plane. The primary potential core length, x_p , is defined as the length downstream of the plug tip at which the local maximum velocity falls to 90% of the core exit velocity. The end of the potential core is of interest as it has been identified from phased array measurements that the strongest noise sources originate from this region.⁹ For the baseline case the potential core length $x_p/D_f = 4.5$.

The mean flow results for the configuration consisting of a single pair of NACA 0012 airfoil vanes are displayed in Figure 27 corresponding to the acoustic results in Figures 10 and 11. The addition of the vanes causes distorted cross-sections with thickening mainly in the lateral ($\phi = 90$ deg) direction. A decrease in the potential core length to $x_p/D_f = 3.3$ also occurs when the vanes are added. Figure 28 displays contours of maximum radial velocity gradient on the $x - \phi$ plane and the relative change in maximum velocity gradient against the baseline case. It is seen that most of the gradient reduction occurs at $\phi = \pm 90$ deg. This may explain the poor noise reduction in the downward direction and the moderate reduction in the sideline direction. It should also be noted that this 2V configuration employed vanes manufactured in the early stages of our micromachining effort that were not as refined as later versions. This may have produced a “dirtier” flow in the vicinity of the nozzle exit.

The mean flow results for case 4V with symmetric vanes are shown in Figure 29 corresponding to the acoustic results of Figures 12 and 13. The longitudinal cross section plot shows a potential core length $x_p/D_f = 4.1$, which is also reduced from the baseline case. The transverse cross-section plots show the thickening of the plume on the underside of the jet, which displays a thicker region than the 2-vane configuration in the downward direction. This can also be seen in Figure 30 which shows the maximum velocity

gradients and relative change in maximum velocity gradients for this configuration. In the vicinity of the nozzle, the gradients are reduced mostly at $\phi = \pm 60$ deg. However, near the end of the potential core ($x/D_f \sim 5$) there is a uniform reduction in the gradient for $-60 \text{ deg} \leq \phi \leq 60 \text{ deg}$. This is consistent with the roughly-equal noise reductions in the downward and sideline reductions seen in Figures 12 and 13.

The use of cambered airfoils in the 4V configuration gives the mean flow results shown in Figure 31. The corresponding acoustic results are in Figures 14 and 15. In comparison to the 4V case with symmetric vanes (Figure 29), the velocity contours are similar but slightly thickened in the lateral direction. Indeed the maximum velocity gradient contour plots, Figure 32, show a slightly larger decrease in gradient at azimuth angles in the vicinity of ± 60 deg which is consistent with the better sideline acoustic results of this configuration.

The effects of using the mesh flaps as a fan flow deflector are evident in the mean flow results in Figure 33, which correspond to the acoustic results in Figures 17 and 18. A strong deflection is evident in the vicinity of the wedge and a thickening of the plume develops either side of the wedge on the top of the jet. This region migrates around the jet several fan diameters downstream to form a thicker region on the underside of the jet which results in the noise reductions presented in the previous section that are better in the downward direction than in the sideline direction. The potential core length for this configuration is $x_p/D_f = 4.2$, a small reduction from the baseline. The reduction in maximum velocity gradient, which can be seen in Figure 34, is reasonably uniform over all azimuth angles except near the top of the jet ($\phi = 180$ deg) where strong gradients are evident very close to the nozzle exit.

The configuration consisting of both the mesh wedge and 2 pairs of cambered vanes (4V+W), corresponding to the acoustic results in Figures 20 and 21 produces the mean flow results shown in Figure 35. The same velocity contour features from the previous two configurations are evident, with a large low speed region on the underside of the jet as a result of both the cambered vanes and the displaced flow from the mesh flaps. A decreased potential core length from the previous two configurations $x_p/D_f = 3.8$ is realized. Figure 36 indicates that significant reductions in the maximum velocity gradient are concentrated in the downward direction in the vicinity of the end of the potential core, consistent with the noise reductions measured in the acoustic experiments.

One of the goals of this research is to correlate changes in the mean velocity, induced by the fan flow deflectors, the corresponding changes in acoustics. The maximum velocity gradient is evidently an important mean flow parameter that has implications for jet noise reduction. Figure 37 shows the correlation between the maximum gradient measured in the downward and sideline directions and the reduction in peak OASPL in the same directions. The maximum velocity gradient was averaged over 2.7 to 5.4 fan nozzle diameters downstream of the plug tip. A general negative trend is realized indicating the importance of producing a thick low speed region around a large range of azimuth angles on the underside of the jet plume in order to give significant acoustic reductions in both downward and sideline directions. The trends in Figure 37 represent our first attempt to correlate noise with flow gradients and in the future we will be seeking improvements in those correlations.

VIII. Conclusion

We report the initial phase of our research on fan flow deflectors for jet noise reduction in next-generation supersonic turbofan engines. An engine cycle analysis was performed to determine reasonable ranges for the bypass ratio, fan pressure ratio, and takeoff exhaust conditions. A cycle with BPR=2.7 and FPR=2.2 was selected. The parametric investigation of fan flow deflectors used acoustic experiments in conjunction with mean velocity surveys to determine the efficacy of several different deflector technologies. Symmetric and cambered micromachined airfoil internal vanes were employed. In addition, an external wedge-type perforated flap deflector was tried. Significant reductions were achieved with all methods however several pertinent trends were realized:

- Internal vanes gave superior noise reduction when they were placed at azimuth angles greater than or equal to 90 deg, which produces thick low speed region on the underside of the jet that extends to the downward direction and sideline direction.
- Two pairs of internal vanes produced a more uniform low speed region on the underside of the jet plume compared to a single pair of vanes. This resulted in superior noise reduction in both downward and sideline directions.

- Vanes with a cambered airfoil section gave superior acoustic results over those with a symmetric airfoil section possibly due to the higher lift to drag ratios of the cambered airfoil. A smaller vane angle of attack can be used for the cambered airfoil giving a lower relative blockage of the fan duct.
- A deployable wedge with a solidity of 0.5 gave significant noise reductions, particularly in the downward direction and produced a uniform low speed region on the underside of the jet.
- Superior noise reductions in both the downward and sideline directions was achieved with a combination of two pairs of cambered airfoil vanes and a mesh wedge. This configuration resulted in cumulative EPNL and OASPL reductions of 7.7 dB and 9.2 dB respectively.
- A general positive trend between deflector turning effort and noise reduction was found. In addition, there is a fair correlation between the reduction in peak OASPL and the reduction of the maximum radial velocity gradient on the underside of the jet near the end of the primary potential core.

Acknowledgments

The support by NASA Cooperative Agreement NNX07AC62A (monitored by Mr. Tom Norum) is gratefully acknowledged. We thank Mr. An Vu for his assistance with the design and fabrication of the vanes.

References

- ¹Papamoschou, D., "Engine Cycle Exhaust Configuration for Quiet Supersonic Propulsion," *AIAA Journal of Propulsion and Power*, Vol. 20, No. 2, 2004, pp. 255–262.
- ²Papamoschou, D., "Fan Flow Deflection in Simulated Turbofan Exhaust," *AIAA Journal*, Vol. 44, No. 12, 2006, pp. 3088–3097.
- ³Zaman, K., Bridges, J., and Papamoschou, D., "Offset Stream Technology - Comparison of Results from UCI and GRC Experiments," AIAA Paper 2007-0438, January 2007.
- ⁴Papamoschou, D., "Pylon Based Fan Flow Deflectors," AIAA Paper 2008-0040, January 2008.
- ⁵Murayama, T., Papamoschou, D., and Liu, F., "Aerodynamics of Fan flow Deflectors for Jet Noise Suppression," AIAA Paper 2005-0994, January 2005.
- ⁶Papamoschou, D., Vu, A., and Johnson, A., "Aerodynamics of Wedge-Shaped Deflectors for Jet Noise Reduction," AIAA Paper 2006-3655, June 2006.
- ⁷Papamoschou, D., "Acoustic Simulation of Hot Coaxial Jets Using Cold Helium-Air Mixture Jets," *AIAA Journal of Propulsion and Power*, Vol. 23, No. 2, 2007, pp. 375–381.
- ⁸Ffowcs-Williams, J., Simson, J., and Virchis, V., "Crackle: an Annoying Component of Jet Noise," *Journal of Fluid Mechanics*, Vol. 71, No. 2, 1975, pp. 251–271.
- ⁹Narayanan, S., Barber, T., and Polak, D., "High Subsonic Jet Experiments: Turbulence and Noise Generation Studies," *AIAA Journal*, Vol. 40, No. 3, 2002, pp. 430–437.

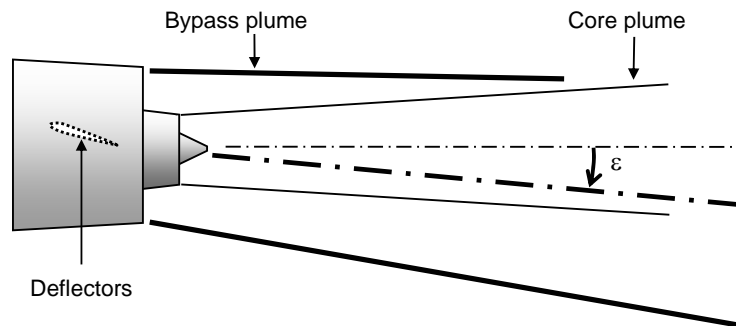


Figure 1. General concept of fan flow deflection.

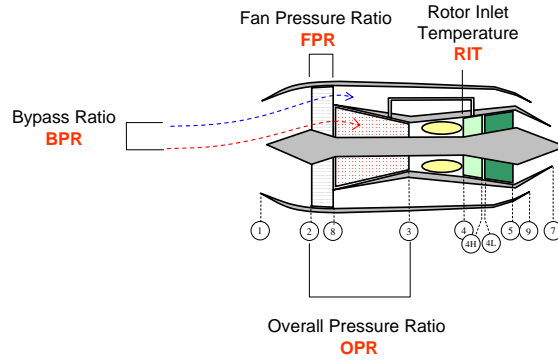


Figure 2. Turbofan engine model used in the thermodynamic cycle analysis.

Table 1. Component efficiencies and specific heat ratios assumed for the $BPR = 2.7$ engine.

	Efficiency η	Specific Heat Ratio γ
Diffuser	0.97 for $M < 0$ 0.85 for $M > 0$	1.40
Fan	0.85	1.39
Compressor	0.85	1.37
Turbine	0.90	1.33
Core Nozzle	0.97	1.36
Fan Nozzle	0.97	1.39

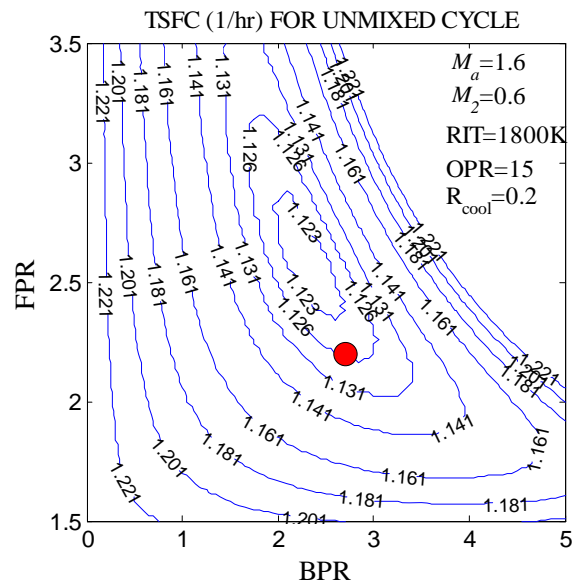


Figure 3. Example result of cycle analysis for Mach 1.6 cruise. Contour maps of thrust specific fuel consumption versus bypass ratio and fan pressure ratio. Red dot indicates design selected.

Table 2. Exhaust conditions for $BPR = 2.7$ nozzle.

	Acoustic Tests	Mean Velocity Surveys
$U_p[m/s]$	600	319
M_p	1.03	1.03
NPR_p	2.00	1.96
$U_s[m/s]$	400	213
M_s	1.15	0.65
NPR_s	2.25	1.33
A_s/A_p	1.40	1.40
U_s/U_p	0.67	0.67

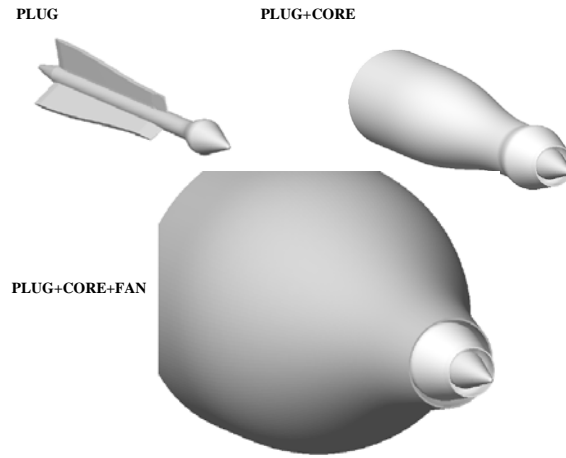


Figure 4. Stereolithography files of the nozzle components and their assembly.

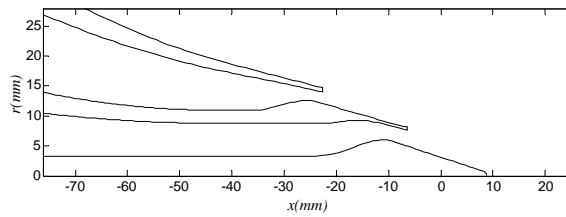


Figure 5. Coordinates of bypass ratio $BPR = 2.7$ (B27) nozzle.

Table 3. Vane and wedge configurations.

Experiment		Vaness					Wedge	
Number	Type	Aifoil	ϕ_1	ϕ_2	α_1	α_2	Material	α_w
108	2V	0012	150		7.5			
124	4V	0012	90	150	7.5	7.5		
142	4V	4412	90	150	7.5	4		
144	W						mesh	20
152	4V+W	4412	90	150	7.5	4	mesh	20

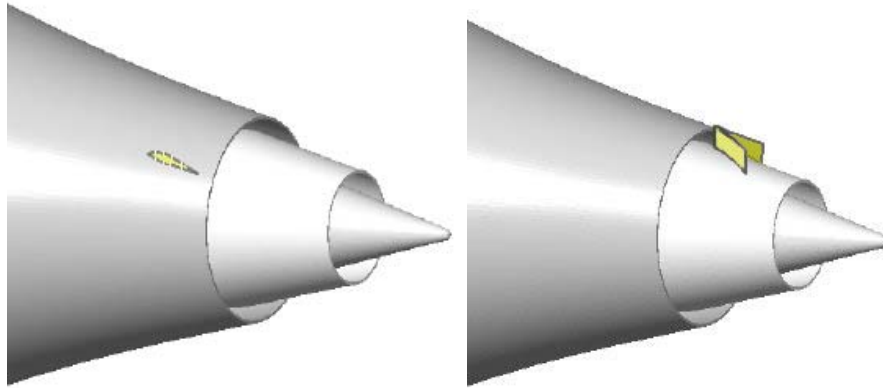


Figure 6. Illustration of internal vane (left) and external wedge/flap (right) fan flow defectors.

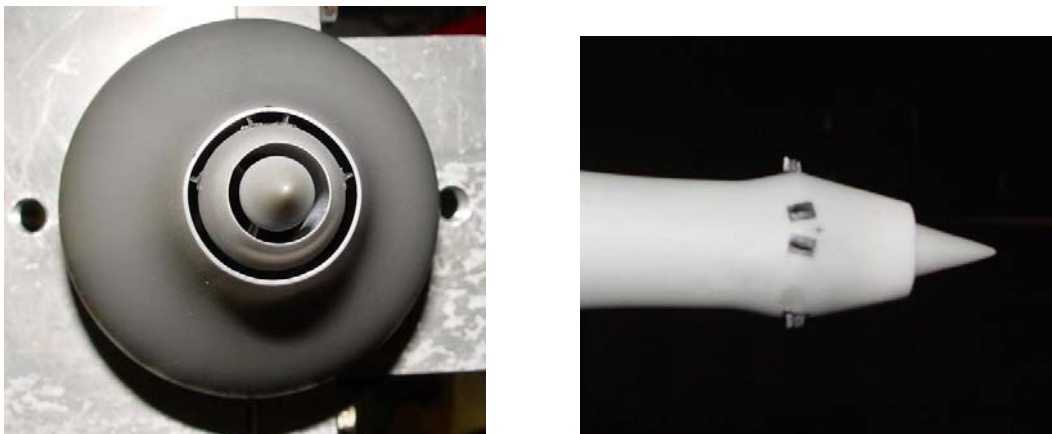


Figure 7. Front and top view (without the fan nozzle) of a 4-vane nozzle configuration.

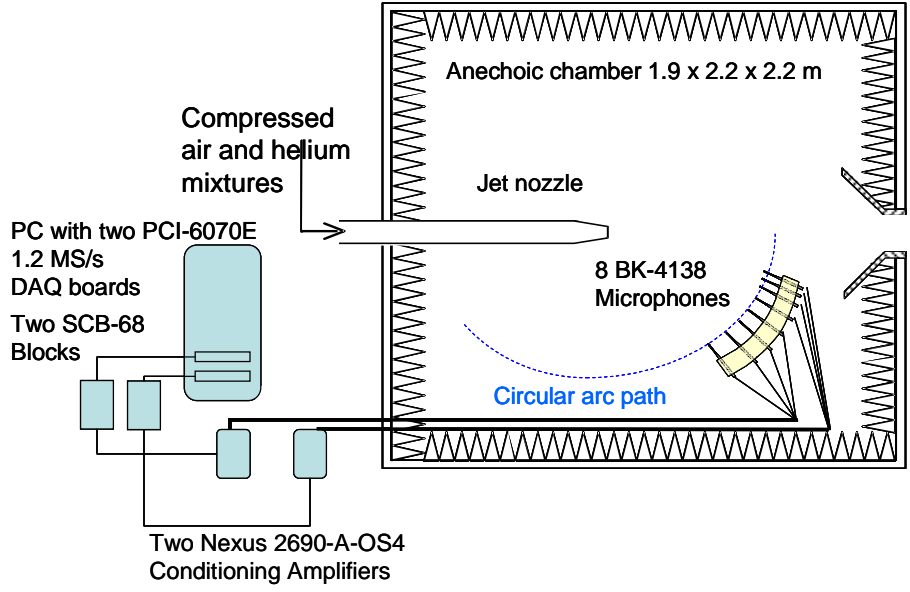


Figure 8. UCI Jet Aeroacoustics Facility.

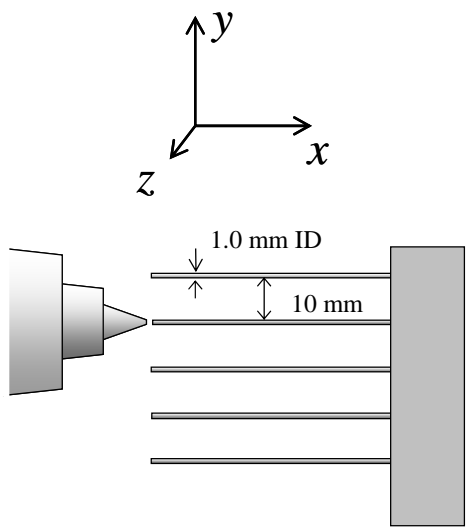


Figure 9. The Pitot traverse system in the Supersonic Mean Flow Facility.

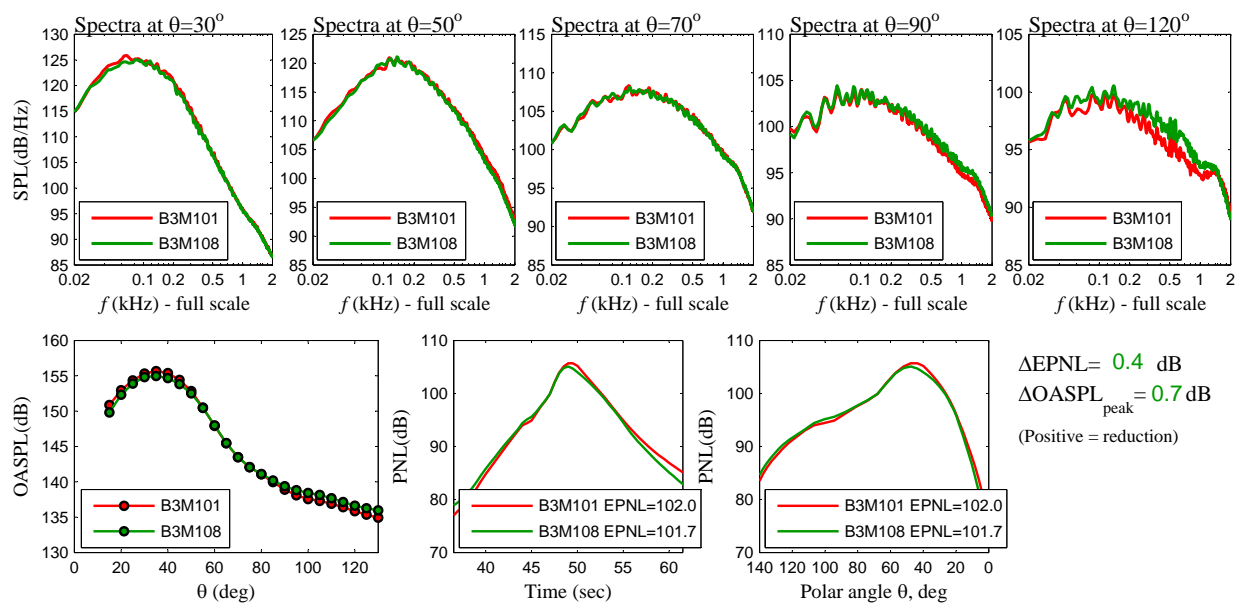


Figure 10. Acoustic results for symmetric 2-vane configuration (2V) with comparison to baseline. Microphone azimuth angle $\phi = 0$ deg (downward).

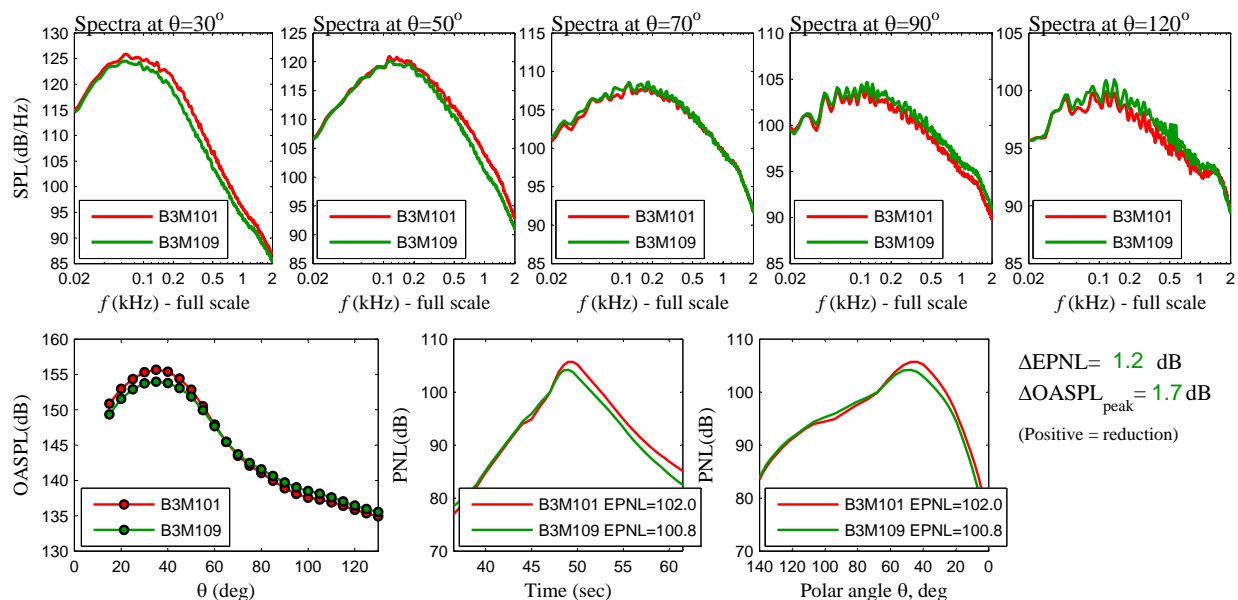


Figure 11. Acoustic results for symmetric 2-vane configuration (2V) with comparison to baseline. Microphone azimuth angle $\phi = 60$ deg (sideline).

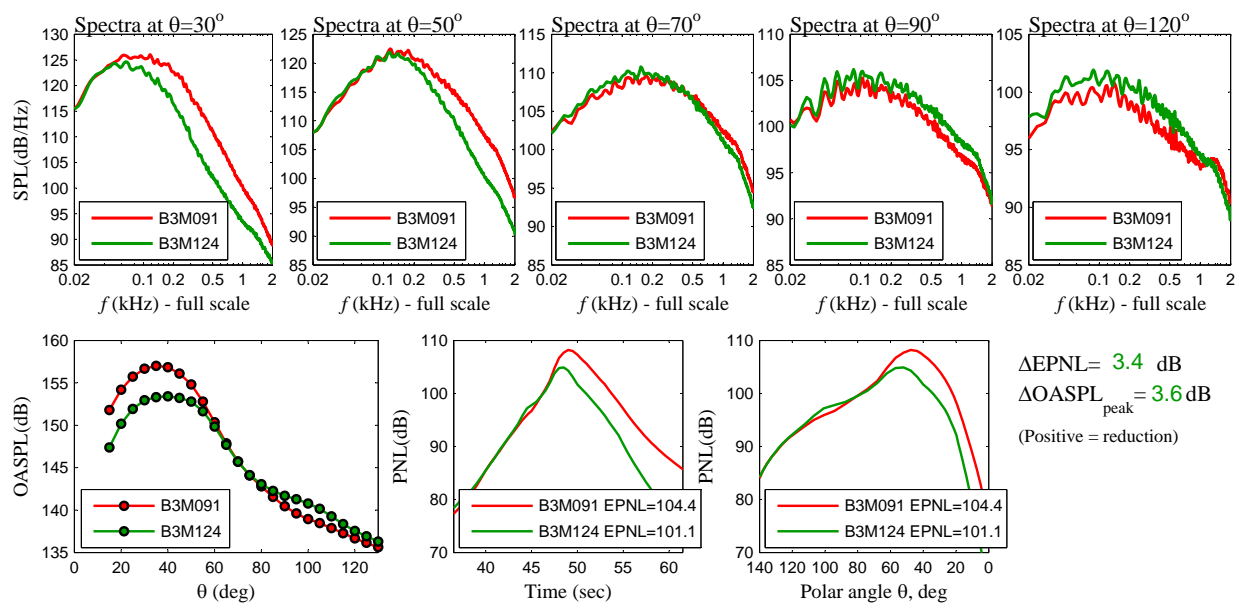


Figure 12. Acoustic results for symmetric 4-vane configuration (4V) with comparison to baseline. Microphone azimuth angle $\phi = 0$ deg (downward).

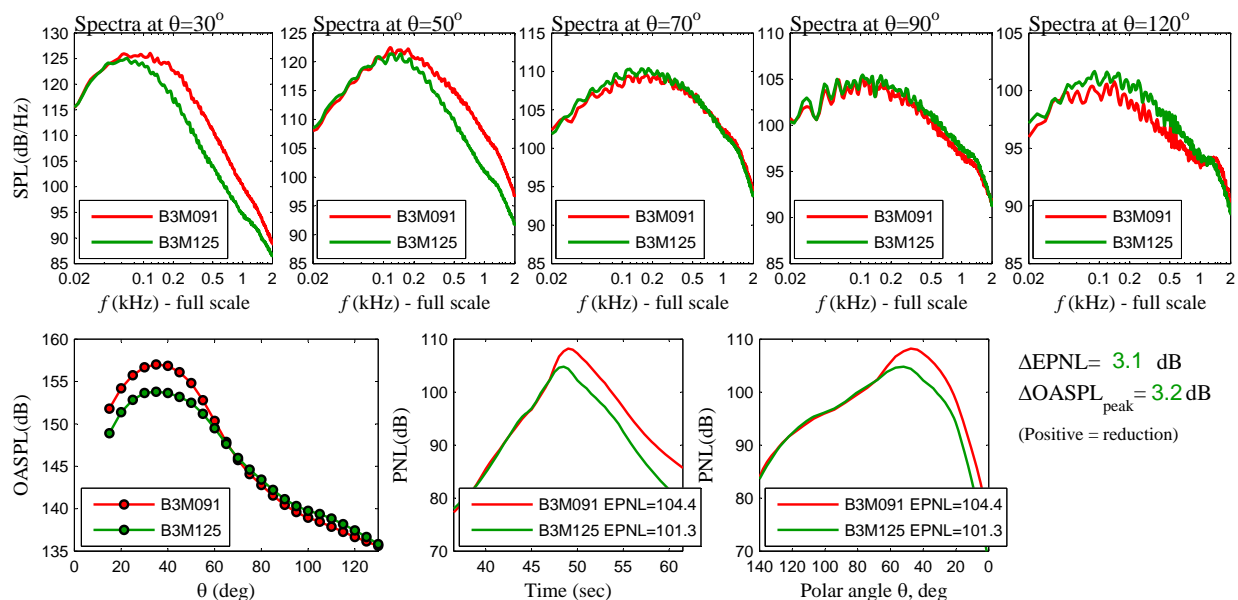


Figure 13. Acoustic results for symmetric 4-vane configuration (4V) with comparison to baseline. Microphone azimuth angle $\phi = 60$ deg (sideline).

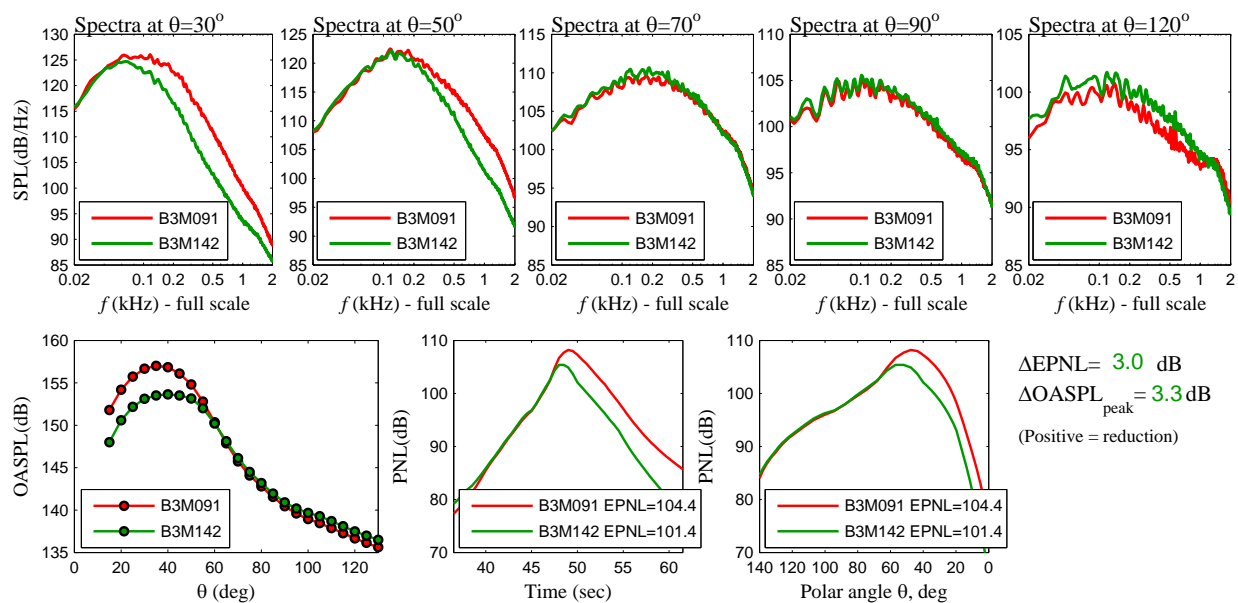


Figure 14. Acoustic results for cambered 4-vane configuration (4V) with comparison to baseline. Microphone azimuth angle $\phi = 0$ deg (downward).

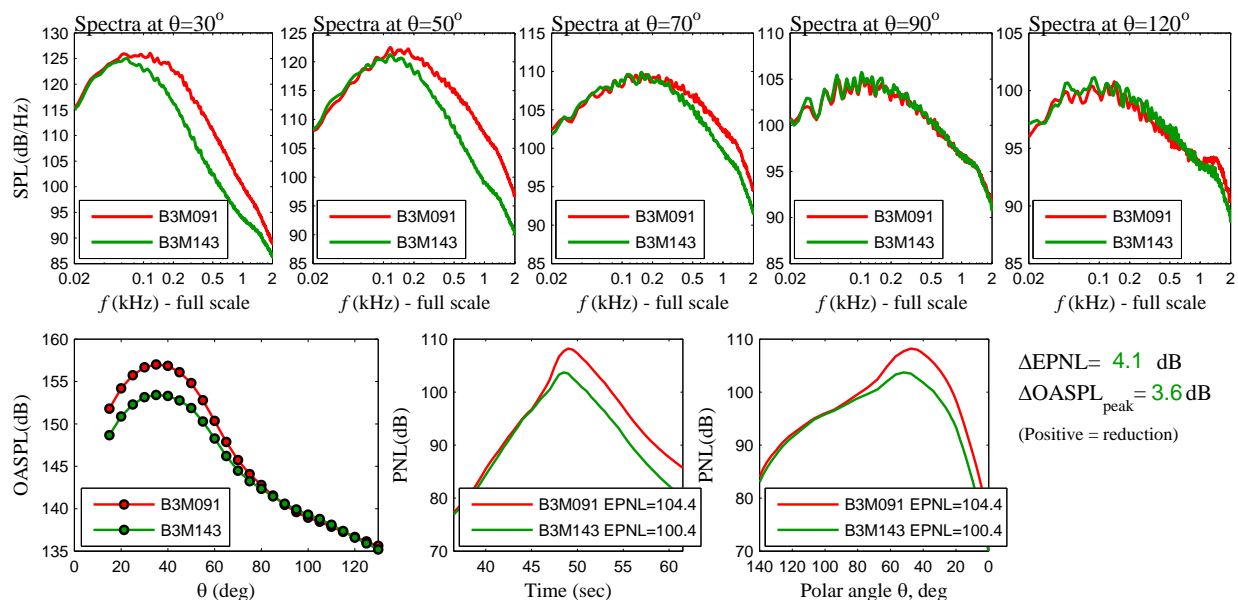


Figure 15. Acoustic results for cambered 4-vane configuration (4V) with comparison to baseline. Microphone azimuth angle $\phi = 60$ deg (sideline).

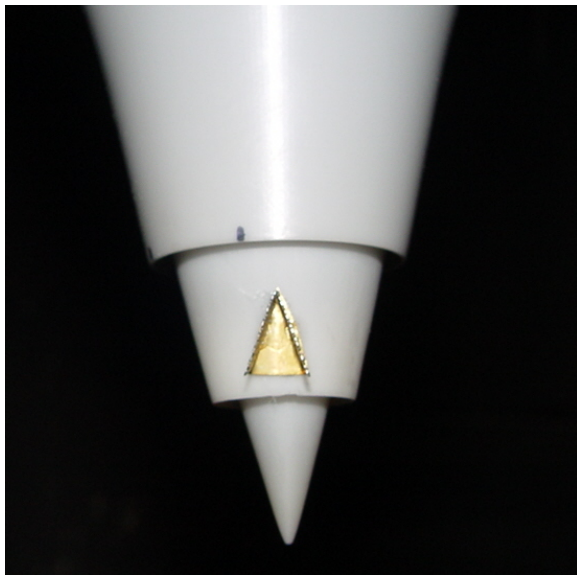


Figure 16. Mesh wedge configuration.

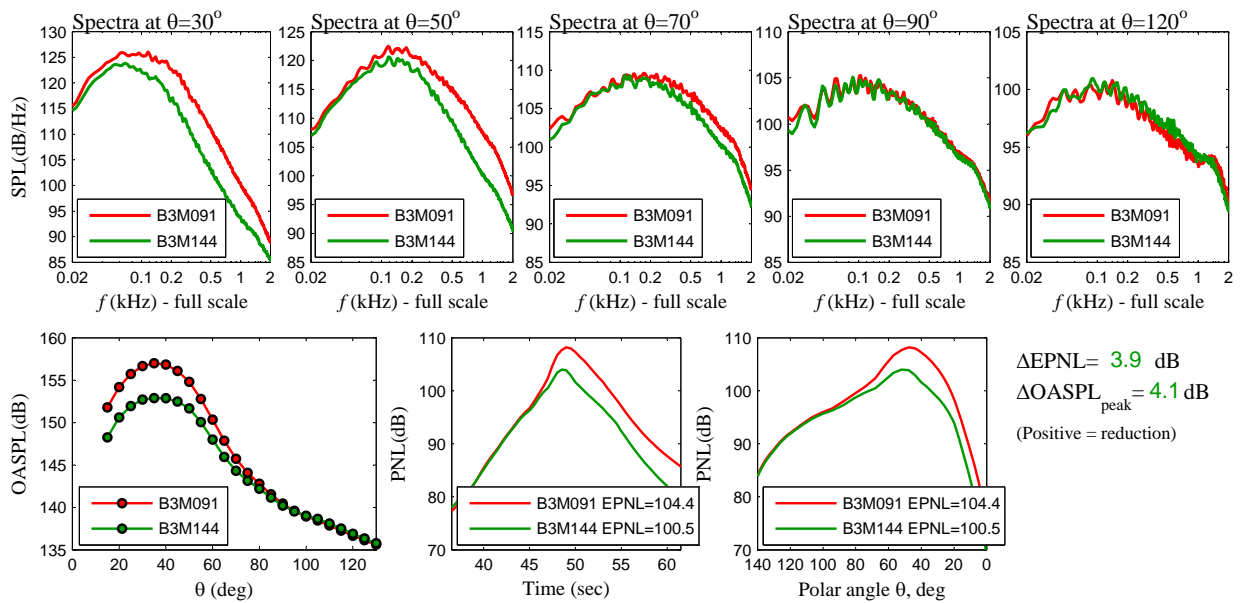


Figure 17. Acoustic results for mesh wedge configuration (W) with comparison to baseline. Microphone azimuth angle $\phi = 0$ deg (downward).

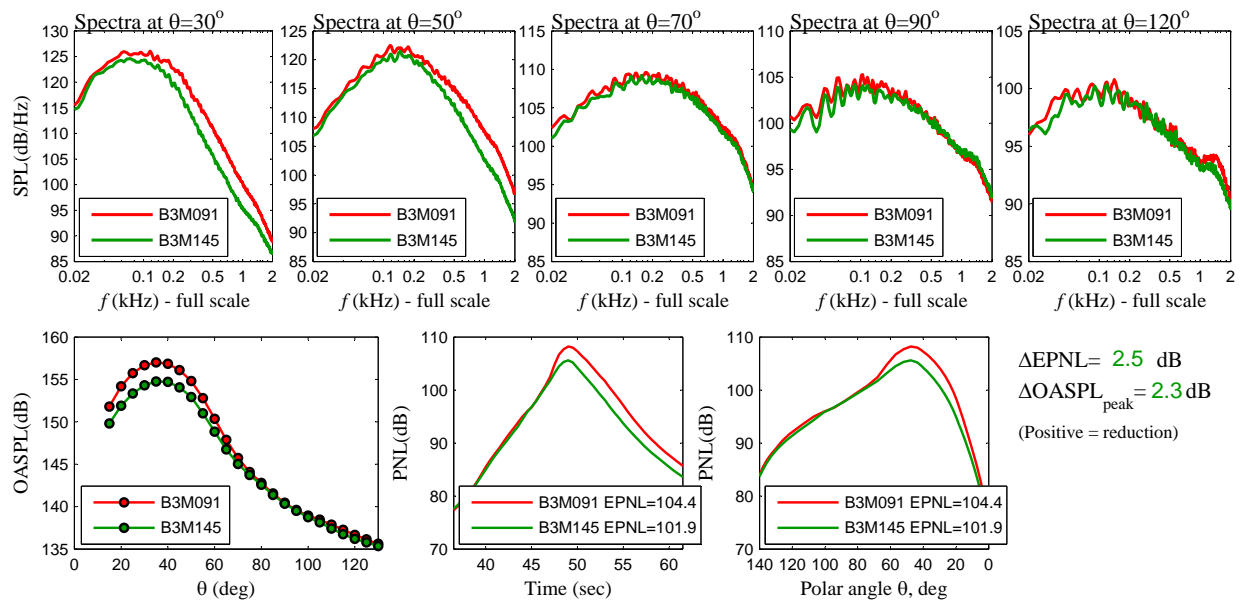


Figure 18. Acoustic results for mesh wedge configuration (W) with comparison to baseline. Microphone azimuth angle $\phi = 60$ deg (sideline).



Figure 19. Cambered 4-vane and mesh wedge configuration.

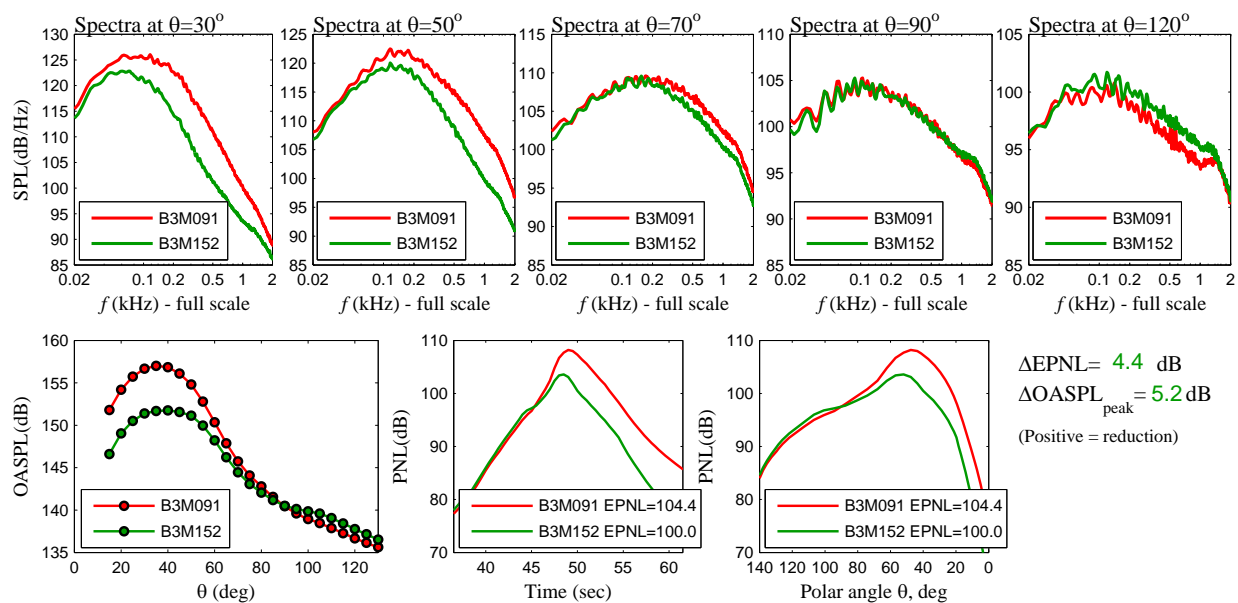


Figure 20. Acoustic results for cambered 4-vane and mesh wedge configuration (4V+W) with comparison to baseline. Microphone azimuth angle $\phi = 0$ deg (downward).

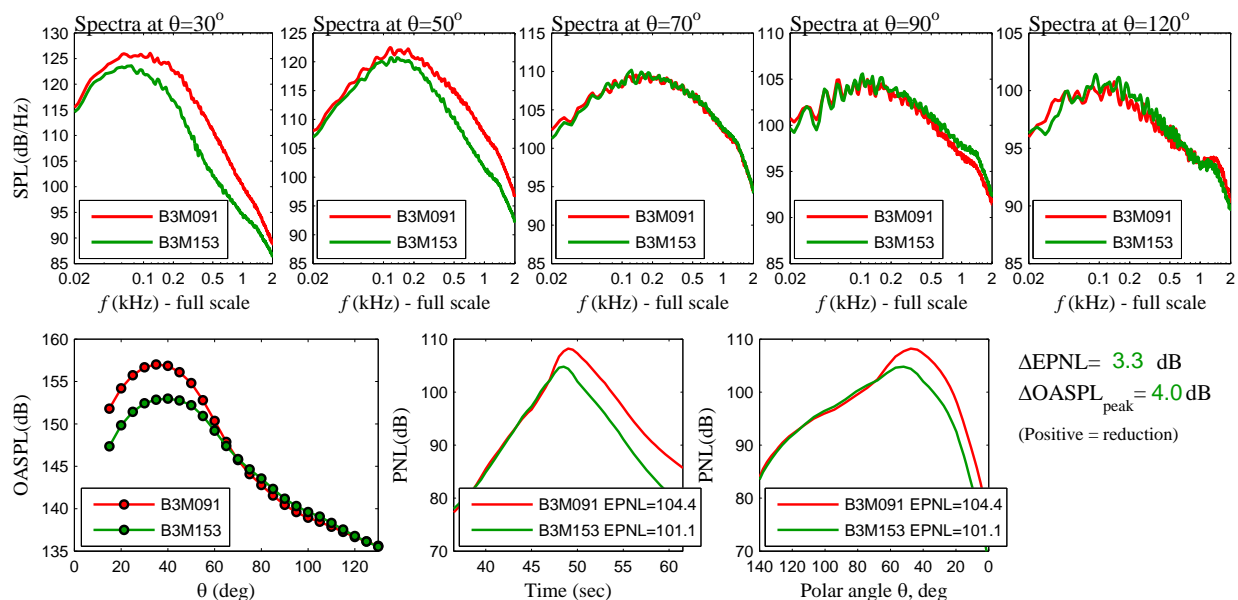


Figure 21. Acoustic results for cambered 4-vane and mesh wedge configuration (4V+W) with comparison to baseline. Microphone azimuth angle $\phi = 60$ deg (sideline).

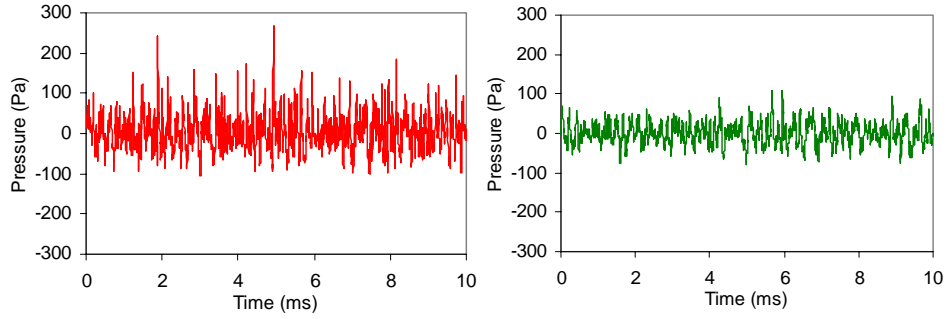


Figure 22. Timetraces of the microphone pressure for the baseline (left) and 4-vane and wedge (right) configurations at $\theta = 40$ deg.

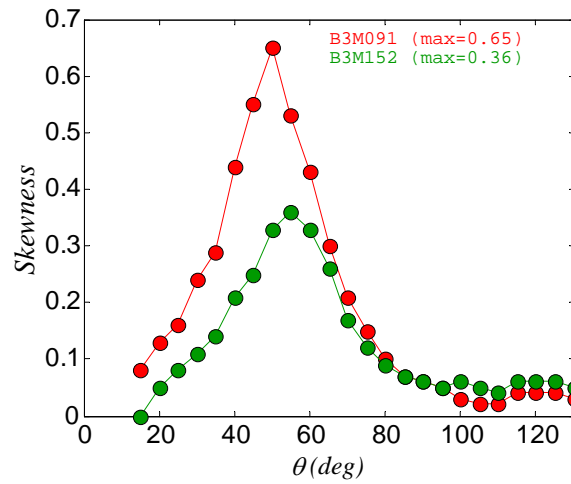


Figure 23. The directivity of the skewness for the baseline and 4-vane plus wedge configurations.

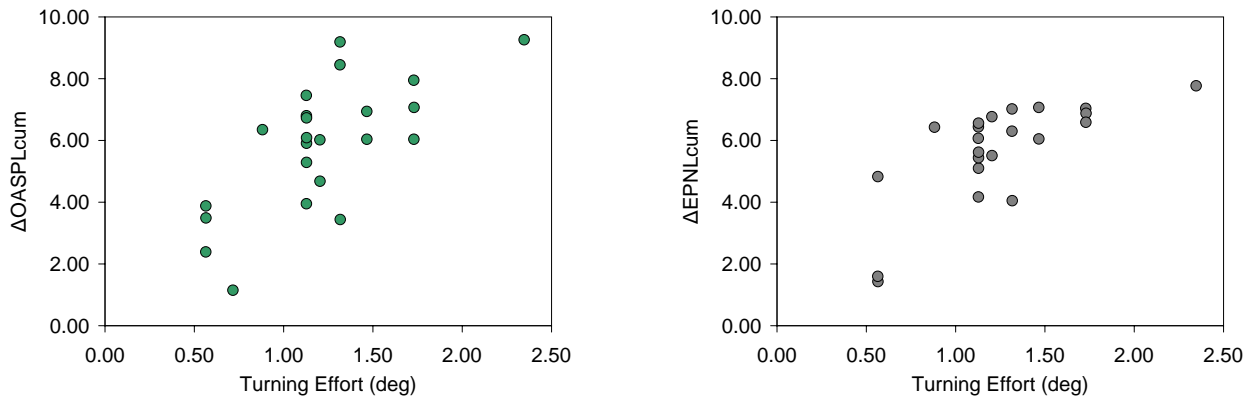


Figure 24. The effect of turning effort on cumulative OASPL (left) and cumulative EPNL (right).

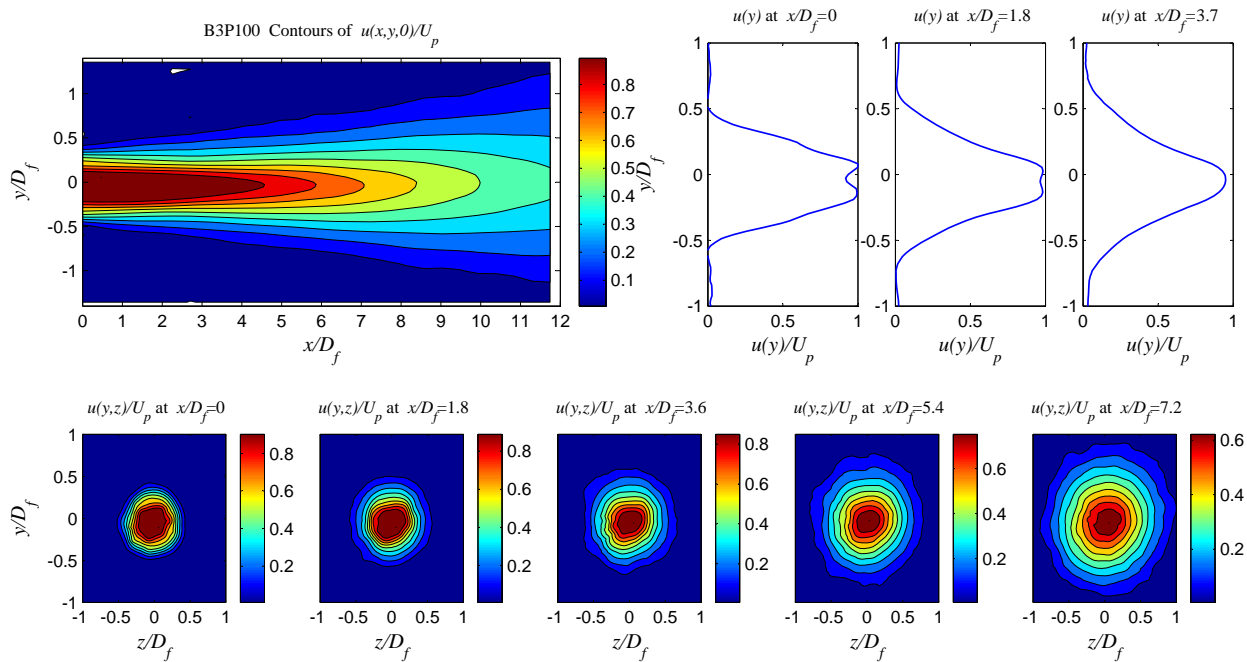


Figure 25. Mean flow results for baseline nozzle.

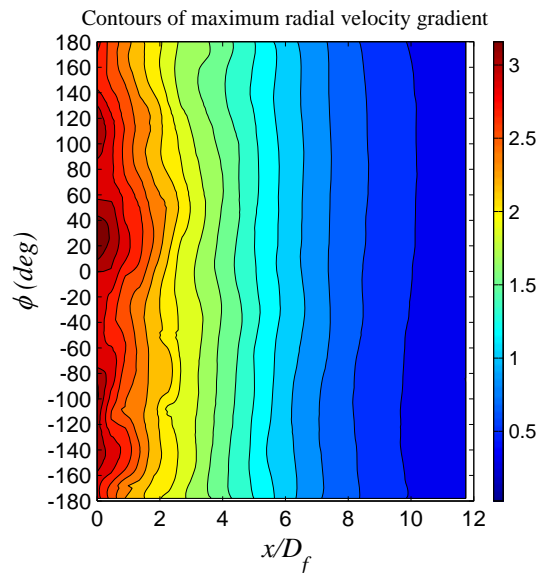


Figure 26. Contours of maximum velocity gradient on $x - \phi$ plane for baseline jet.

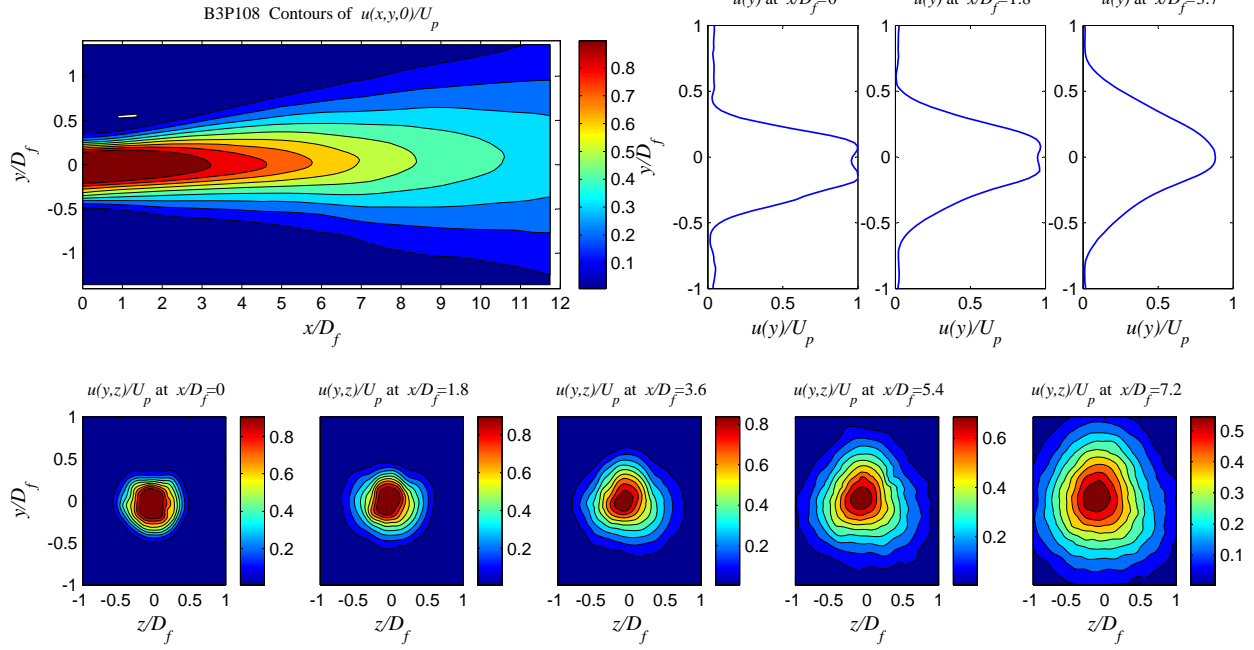


Figure 27. Mean velocity results for symmetric 2-vane configuration (2V).

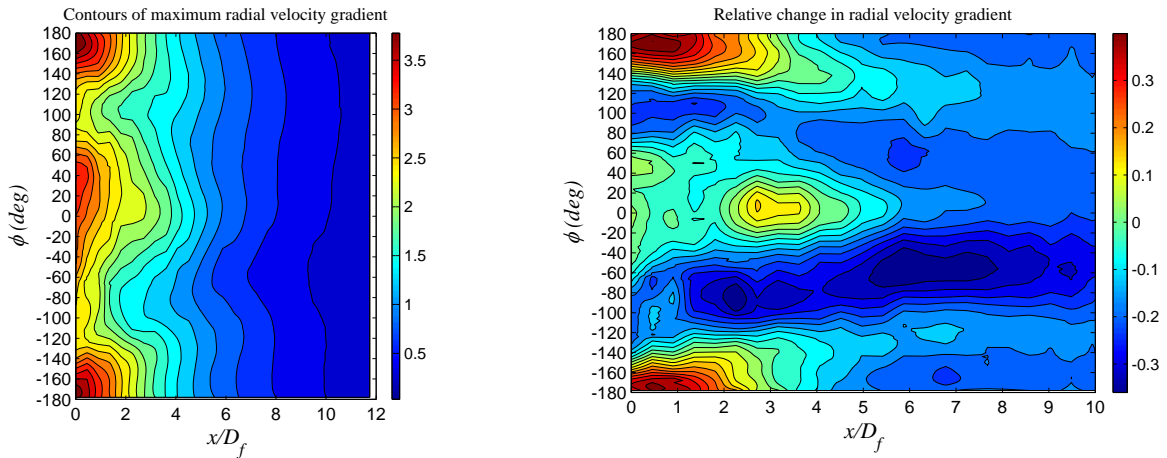


Figure 28. Contours of maximum radial velocity gradient on $x-\phi$ plane shown in absolute (left) and differential (right) forms for symmetric 2-vane configuration (2V).

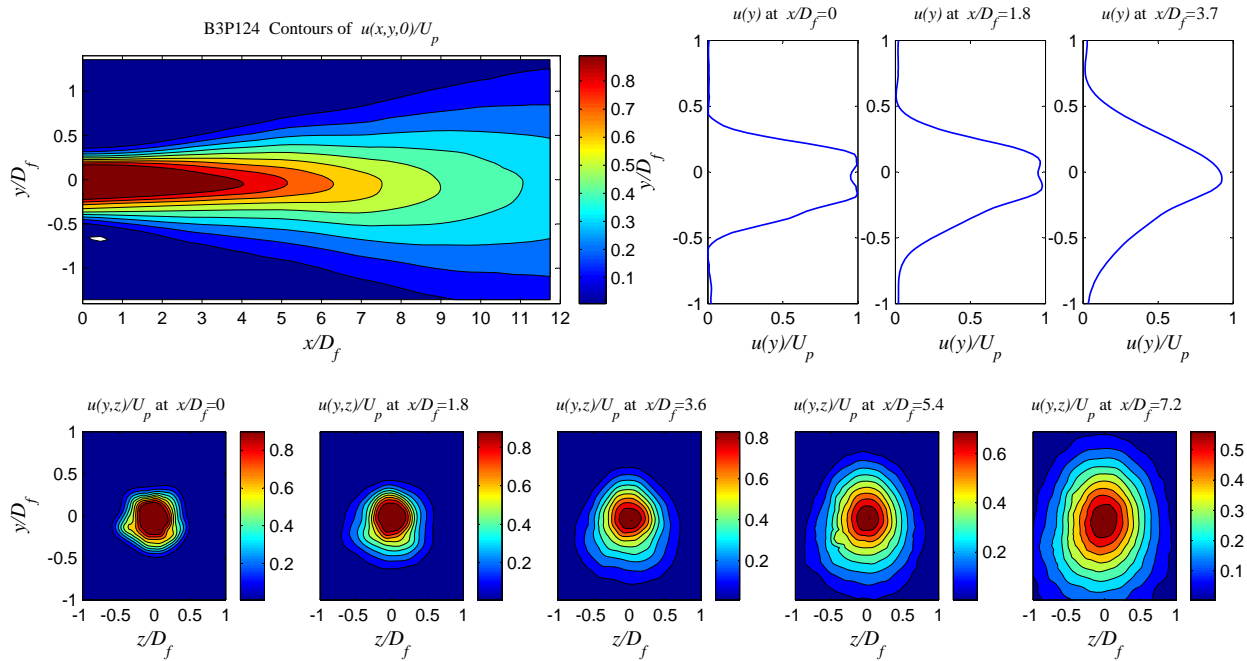


Figure 29. Mean velocity results for symmetric 4-vane configuration (4V).

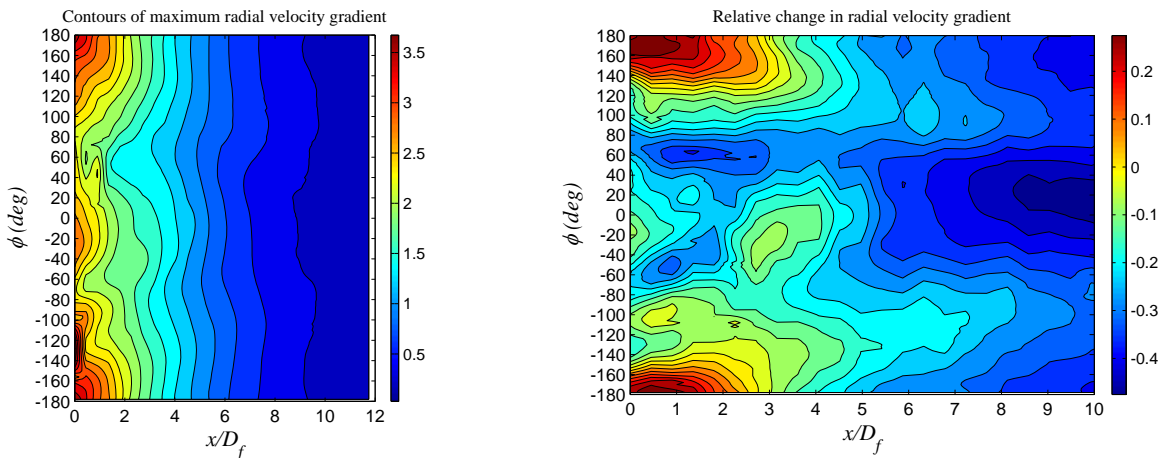


Figure 30. Contours of maximum radial velocity gradient on $x-\phi$ plane shown in absolute (left) and differential (right) forms for symmetric 4-vane configuration (4V).

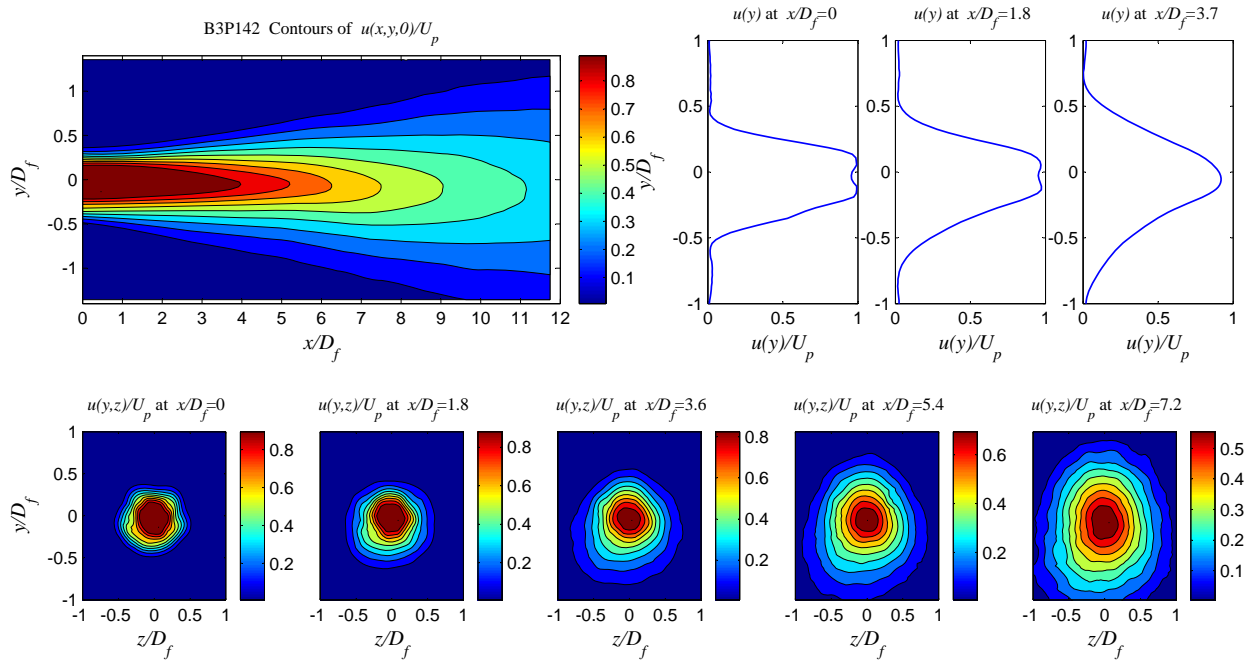


Figure 31. Mean velocity results for cambered 4-vane configuration (4V).

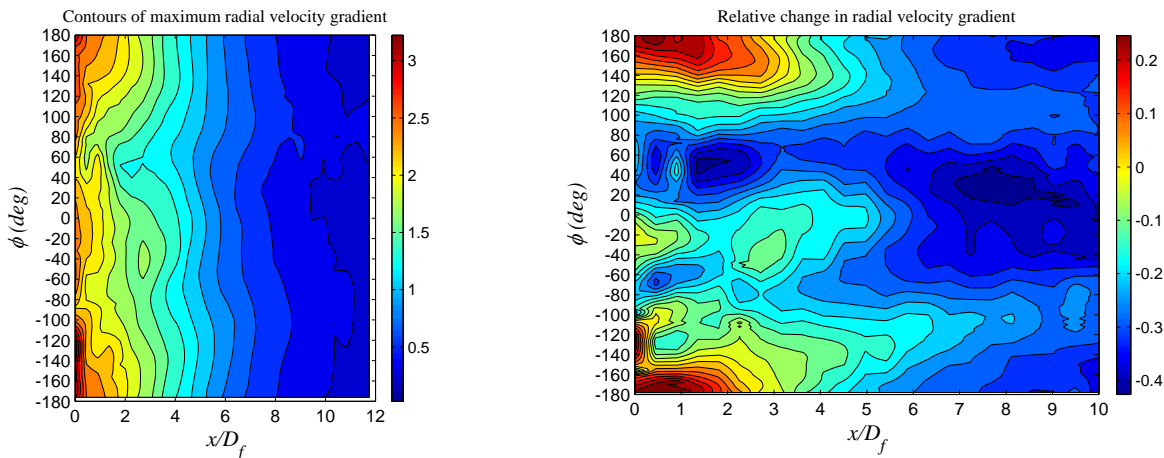


Figure 32. Contours of maximum radial velocity gradient on $x-\phi$ plane shown in absolute (left) and differential (right) forms for cambered 4-vane configuration (4V).

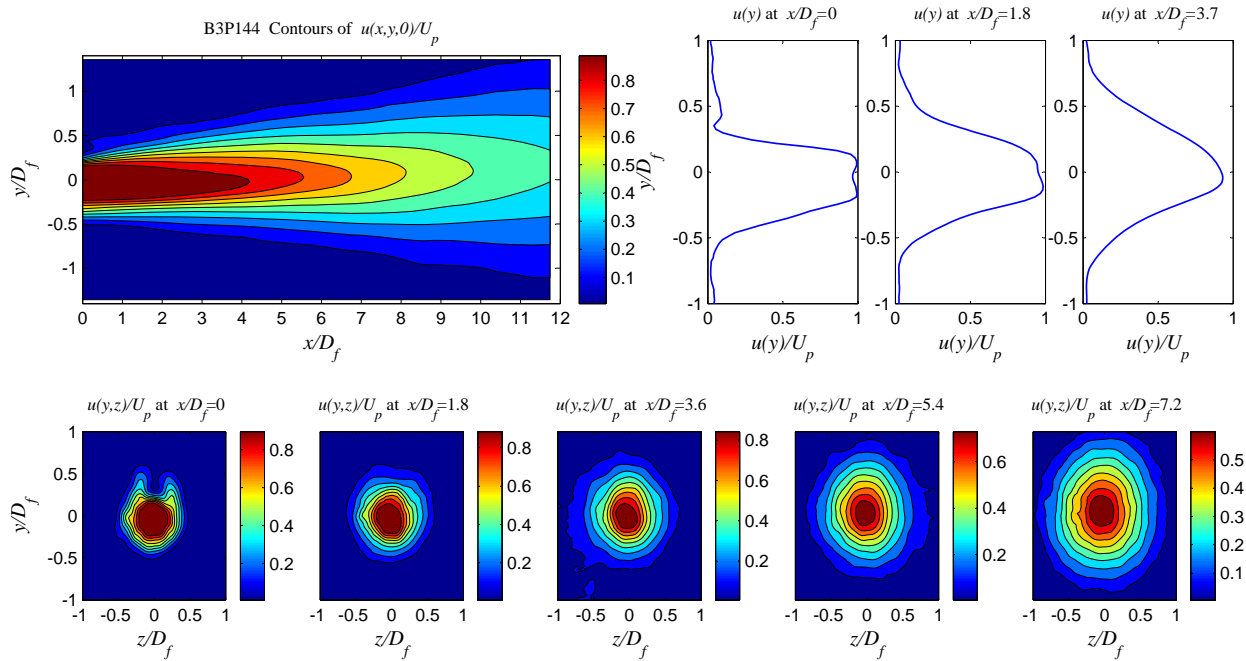


Figure 33. Mean velocity results for mesh wedge configuration (W).

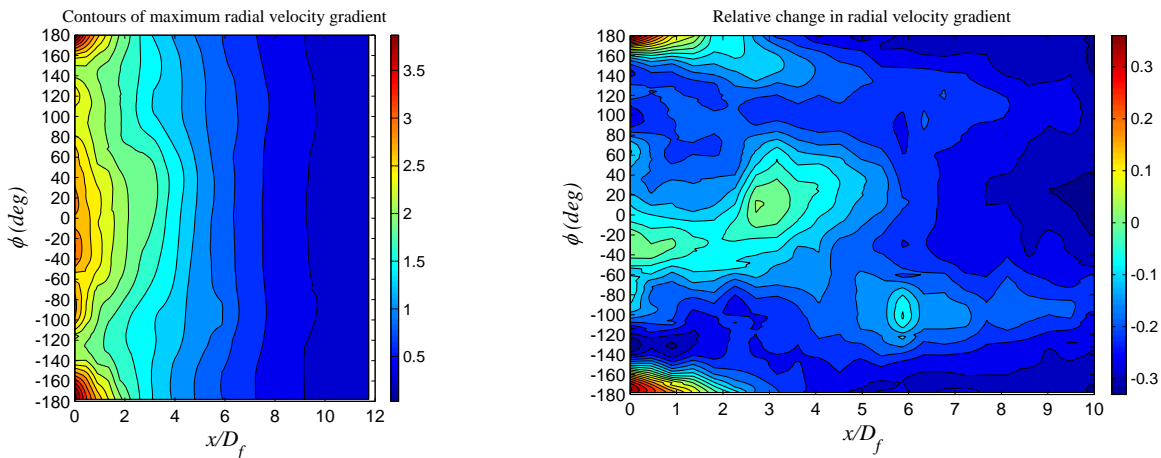


Figure 34. Contours of maximum radial velocity gradient on $x-\phi$ plane shown in absolute (left) and differential (right) forms for mesh wedge configuration (W).

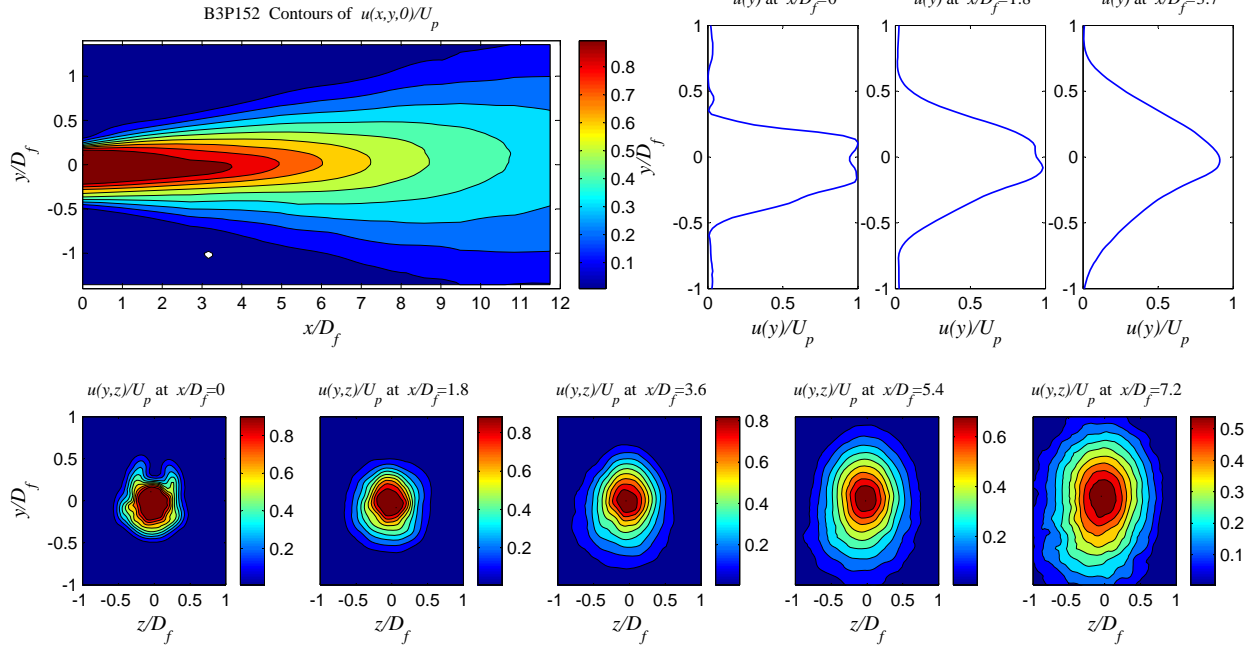


Figure 35. Mean velocity results for cambered 4-vane and mesh wedge configuration (4V+W).

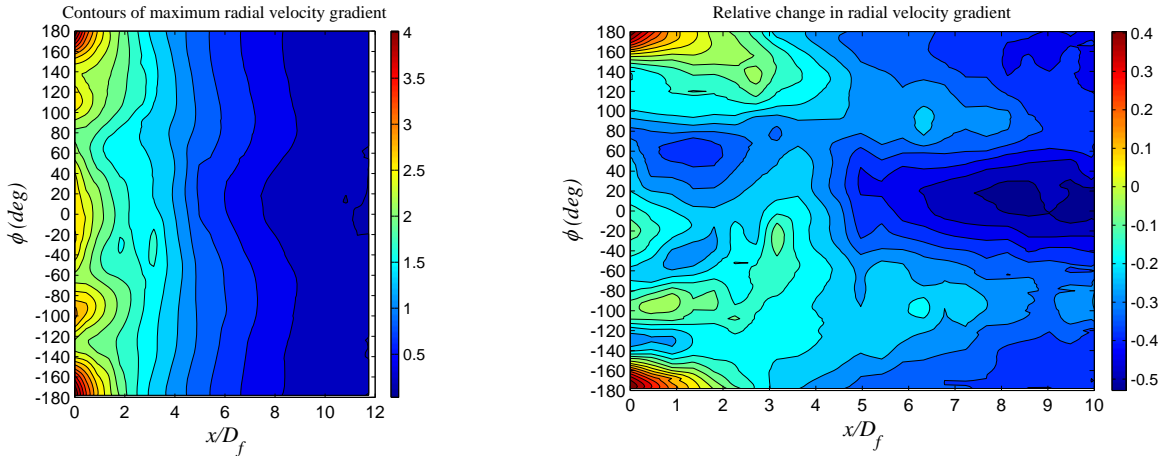


Figure 36. Contours of maximum radial velocity gradient on $x-\phi$ plane shown in absolute (left) and differential (right) forms for cambered 4-vane and mesh wedge configuration (4V+W).

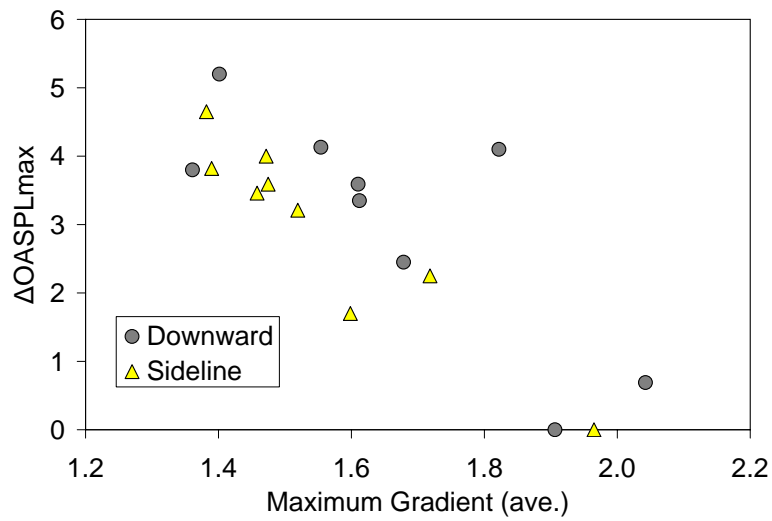


Figure 37. Correlation of suppression in peak OASPL with reduction of maximum radial velocity gradient G_{max} averaged over the axial extent $2.7 < x/D_f < 5.4$.